Research Square

Preprints are preliminary reports that have not undergone peer review.
They should not be considered conclusive, used to inform clinical practice,
or referenced by the media as validated information.

Evaluation of the Enhanced Constrained Rod Casting Test for Hot Tearing of 7xxx Aluminium Alloys

Zheng Gong
Kunming University of Science and Technology
Qing Yu
Kunming University of Science and Technology
Lianjian Wen
Kunming University of Science and Technology
Mingjun Peng
Kunming University of Science and Technology
Jianjun Yao
gjjb@163.com

Chinalco (Yunnan) Green Advanced Aluminum-based Materials Co.
Hongmei Yang
Kunming University of Science and Technology
Mengnie Li
Kunming University of Science and Technology

Research Article

Keywords: hot tearing, enhanced constrained rod casting (ECRC), 7xxx aluminium alloy, Kou criterion, numerical simulation, Fe-rich intermetallics

Posted Date: August 27th, 2026

DOI: https://doi.org/10.21203/rs.3.rs-10401599/v1

License: This work is licensed under a Creative Commons Attribution 4.0 International License.
Read Full License

Additional Declarations:
No competing interests reported.

Table 3 is not available with this version

Version of Record: A version of this preprint was published at International Journal of Metalcasting on October 31st, 2026. See the published version at https://doi.org/10.1007/s40962-026-02190-0.

Evaluation of the Enhanced Constrained Rod Casting Test for Hot Tearing of 7xxx Aluminium Alloys

Zheng Gong [a,1],Qing Yu [a,c,1],Lianjian Wen [a,c],Mingjun Peng [a],Jianjun Yao [b,*],Hongmei Yang [a,**],Mengnie Li [a,***]

[a] Faculty of Materials Science and Engineering, Yunnan Key Laboratory of Integrated Computational Materials Engineering for Light Alloys, Kunming University of Science and Technology, Kunming 650093, China.

[b] Chinalco (Yunnan) Green Advanced Aluminum-based Materials Co., Ltd.

[c] Yunnan Aluminum Hai Xin Aluminum Co., Ltd., Kunming 650031, Yunnan, China

[*] Corresponding author.

[**] Corresponding author.

[***] Corresponding author.

[1] These authors contributed equally to this work and should be considered co-first authors.

[2] These authors have made equal contributions to this work and should be considered as co-corresponding authors.

Contact e-mail: Zheng Gong 18396997269@163.com, Qing Yu yu_hxq@163.com, Lianjian Wen wlj624418509@163.com, Mingjun Peng pmj5530594@kmust.edu.cn, Jianjun Yao gjjb@163.com, Hongmei Yang yhmei125@kust.edu.cn, Mengnie Li limengnie@kust.edu.cn

Abstract

The enhanced constrained rod casting (ECRC) test has been validated mainly on narrow-freezing-range alloys such as A206 and A380, and its repeatability and interpretation for wide-freezing-range 7xxx Al–Zn–Mg–Cu alloys remain largely unreported. Here, four cast 7xxx alloys containing 0.081–0.232 wt.% Fe were used as a case series, with three independent ECRC trials per composition. Crack widths, fracture locations, contraction load and temperature were cross-examined against JMatPro–Kou calculations, backscattered-electron/energy-dispersive spectroscopy (BSE/EDS) quantification and elastic–viscoplastic ProCAST simulations. Fracture locations were highly repeatable—the column-end junctions of the short rods A and B fractured in all twelve castings (100%)—whereas the long-rod (C, D) fractures were dispersed. The all-rod hot-tearing susceptibility (HTS) gave means of 67.1 ± 6.7, 74.1 ± 3.8, 68.3 ± 7.9 and 62.7 ± 19.0 for the Base, #1, #2 and #3 alloys; the between-alloy differences were smaller than the casting-to-casting variability and not statistically significant ($p = 0.730$). The peak contraction load was far more repeatable and ranked alloy #1 highest (87.2 ± 3.2 N, $p = 0.077$), as did the Kou index of the measured compositions, whereas a Fe-only scan produced nearly invariant indices—showing that the differences originate from the multicomponent solidification path, not from Fe alone. ProCAST reproduced the longest late-mushy-stage residence and highest accumulated plastic strain at the A/B junctions, matching the 100% fracture frequency; rods C and D solidified first at mid-length, cutting off feeding and making their response geometry-dominated. The ECRC test is thus applicable to 7xxx alloys provided that short-rod and long-rod responses are interpreted separately, and that fracture-location statistics and the load signal—rather than the crack-width score—are used as the evaluation metrics.

Keywords: hot tearing; enhanced constrained rod casting (ECRC); 7xxx aluminium alloy; Kou criterion; ProCAST simulation; Fe-rich intermetallics

1. Introduction

7xxx Al–Zn–Mg–Cu alloys combine low density, high specific strength and good fatigue resistance, and are widely used in aerospace, rail-transit and other lightweight structural applications [1,2]. Large ingots of these alloys are produced by direct-chill (DC) casting followed by homogenisation and thermomechanical processing [2,3]. Because the high Zn, Mg

and Cu contents widen the freezing range, continuous interdendritic liquid films persist into the terminal stage of solidification; when restrained thermal contraction coincides with insufficient liquid feeding, cracks nucleate in the mushy zone and propagate along grain boundaries [4,5]. Hot tearing reduces ingot yield and can act as a latent crack source during subsequent processing and service, and it remains one of the principal defects limiting the stable production of 7xxx ingots [4,6].

A number of criteria have been proposed to quantify hot-tearing susceptibility. The Clyne–Davies criterion relates cracking to the ratio of the vulnerable time interval to the stress-relaxation interval [7]; the Katgerman criterion additionally accounts for dendrite coherency and feeding deficiency [8]; the RDG criterion derives cracking from the pressure drop in the mushy zone [9]. Kou formulated the problem as a competition at the grain boundary between separation by tensile deformation, lateral growth of neighbouring grains and feeding by the residual liquid, and proposed the maximum slope $|dT/d(f_s)^{1/2}|$ near $f_s^{1/2} \rightarrow 1$ as a cracking index [10,11]. This index has been validated on binary and ternary aluminium and magnesium systems [12,13], and because it can be obtained directly from the solidification path, it is widely used as a first screening tool. Nevertheless, all such criteria capture only the solidification-path contribution; in a real casting the local constraint geometry, thermal history and load evolution must be characterised experimentally.

Constrained rod casting (CRC) is the most widely used experimental method for ranking hot-tearing susceptibility, because rods of different lengths impose different levels of restraint [14]. Dubey systematically optimized the gating of the conventional CRC mold and developed the enhanced constrained rod casting (ECRC) mold, which improves the synchronisation of filling and the uniformity of solidification among the rods and integrates force and temperature measurements [15,16]. Subsequent work confirmed that rod orientation, rod length and local geometry strongly influence crack location and severity [17], and weighting schemes based on crack grade, rod length and crack location have been proposed to convert observations into a numerical hot-tearing susceptibility [18]. To date, however, ECRC validations have been reported mainly for A206, A380 and Al–Cu casting alloys [15,16]. Wide-freezing-range 7xxx alloys combine a long vulnerable interval with strong late-stage precipitation, and recent studies on related Al–Zn–Mg–Cu compositions indicate that their filling, contraction and cracking behavior differs from that of narrow-range alloys [19,20]. Repeatability data, fracture-location

statistics and guidance on how to interpret the different rod positions of the ECRC test for this alloy class are still scarce.

Fe is an impurity that cannot be fully eliminated during the melting and casting of 7xxx alloys. It forms Al_3Fe, Al_7Cu_2Fe and related Fe-rich intermetallics whose amount, morphology and distribution depend on Fe content, cooling conditions and the matrix composition [3,21]. Studies on Al–Cu and Al–Mg–Si systems have shown that Fe and Si modify hot tearing through changes in Fe-rich phase morphology and feeding, and that the effect can be non-monotonic with Fe content [21–23]; recent work on 5083, 6061 and 7075 ingots confirmed the coupled action of Fe, Si, Cu and grain refiner [24]. For 7xxx alloys, existing Fe-related studies have focused on mechanical properties, fracture toughness and corrosion of wrought material [25–27], while the as-cast hot-tearing response remains much less documented. A further methodological difficulty is that Fe in practical alloy series rarely varies alone: when Zn, Mg and Cu co-vary with Fe, the solidification path changes as a whole, and attributing the response to Fe alone can be misleading. A four-alloy series spanning 0.081–0.232 wt.% Fe therefore also provides a demanding case study for assessing what the ECRC test can and cannot resolve.

The present work evaluates the ECRC test for hot-tearing characterization of wide-freezing-range 7xxx Al–Zn–Mg–Cu alloys, using the four Fe-containing compositions as a case series. Three independent ECRC trials were performed for each composition, giving twelve instrumented castings. Position-resolved crack and fracture statistics, the contraction-load signal, JMatPro–Kou calculations including a Fe-only sensitivity scan, elastic–viscoplastic (E-VP) ProCAST simulation and SEM/BSE-EDS quantification of Fe-enriched regions were combined to answer three questions: (i) which ECRC observables are repeatable for 7xxx alloys; (ii) how the responses of the short rods (A, B) and the long rods (C, D) should be interpreted; and (iii) whether alloy-to-alloy differences along the tested composition path exceed the inherent variability of the test. The objective is to establish practical guidance for applying the ECRC method to this alloy class, rather than to define a universal critical Fe content.

2. Materials and methods

2.1 Alloy preparation

The experimental alloys were prepared from commercially pure Al with pure Fe, pure Zn, pure Cu and AlMg50 and AlZr5 master alloys, with an AlTiB grain refiner addition. All raw

materials were cleaned and dried before use. Each charge of approximately 1 kg was melted in a 3 kg graphite crucible in a resistance furnace. Pure Al was melted at 680–700 °C; the melt was heated to 740–750 °C and pure Fe and pure Cu were dissolved with stirring; the temperature was lowered to 730–740 °C for the AlZr5 addition followed by a 5 min hold; AlMg50 and pure Zn were added at 710–720 °C with rapid stirring; finally 0.1 wt.% AlTiB refiner was added at 720–730 °C and plunged below the melt surface.

The compositions measured by X-ray fluorescence (XRF) are listed in Table 1. The Fe contents were 0.081, 0.127, 0.166 and 0.232 wt.% for the Base, #1, #2 and #3 alloys, respectively. The Zn, Mg, Cu and Zr contents varied slightly among the alloys; the series therefore follows a measured multicomponent composition path with Fe as the target variable and Zn, Mg, Cu and Zr as covariates. This point is addressed explicitly in Section 2.4 by comparing a Fe-only calculation path with the measured compositions.

Table 1 Measured chemical compositions of the four alloys (wt.%)

Alloy code	Composition					
	Fe	Zn	Mg	Cu	Zr	Al
Base	0.081	7.19	1.52	1.43	0.11	Balance
#1	0.127	7.30	1.57	1.47	0.11	
#2	0.166	7.34	1.57	1.49	0.10	
#3	0.232	7.42	1.58	1.50	0.10	

2.2 ECRC test and repeated trials

The ECRC mold (H13 steel) and the instrumented platform are shown in Figure 1. The mold contains four constrained rods (A, B, C, D) of lengths 30, 55, 100 and 145 mm, a rod diameter of 9.5 mm, a limiting ball of 19 mm diameter at each rod end, a central sprue, and a 170 mm force-measuring rod without a ball end for recording the contraction load; the overall mold dimensions are 285 mm × 247 mm with a half-mold thickness of 35 mm [15]. K-type thermocouples were placed at mold position T1 and at position T2 near the load sensor and were

connected to a HIOKI LR8450 logger; the load signal was recorded by a D800 indicator with a synchronised DAQ system.

Before pouring, the mold cavity was coated with approximately 40 μm of boron nitride (BN). The mold was first heated to 300 °C to dry the coating, remove moisture and stabilise the mold surface, and was then allowed to cool naturally to 200 ± 5 °C, which was the actual pre-pouring mold temperature. The pouring temperature was 710 ± 5 °C; the melt was poured by gravity along the sprue at 0.2–0.4 kg s^{-1}. Castings cooled naturally in the mold and were demolded at approximately 300 °C.

Three independent ECRC trials were performed for each of the four compositions, giving twelve castings in total. For every casting, the crack width, crack location and HTS contribution of each rod, together with the load and temperature histories, were recorded. Results are reported as casting-level mean ± standard deviation (SD); the rods within a casting are treated as nested observations and are not counted as independent replicates.

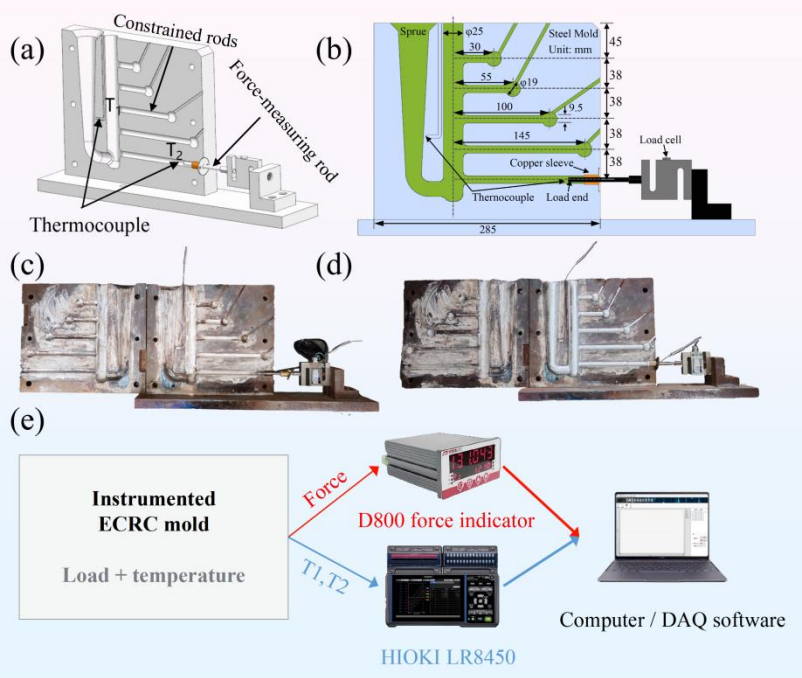


Figure 1. Experimental configuration of the enhanced constrained rod casting (ECRC) test. (a) Three-dimensional schematic of the apparatus showing the constrained rods A–D, the force-measuring rod and the thermocouple positions; (b) dimensional drawing of the mold and

instrumented locations; (c, d) photographs of the mold before and after casting; (e) instrumented platform including the mold, force indicator, temperature logger and data-acquisition computer.

2.3 Crack measurement and hot-tearing susceptibility

After demolding, each casting was photographed under natural light at 1× magnification. The fracture position and the maximum crack width w_{crack} (mm) of each rod were obtained by the same image-analysis procedure; when a rod contained several crack features, the largest width was used. Conventional constrained-rod evaluation assigns weights to crack grade, rod length and fracture location [16,18]. The conventional score is retained here only to document the derivation:

$$HTS' = \sum\left(f_{\mathrm{crack}}\, f_{\mathrm{length}}\, f_{\mathrm{location}}\right)$$

where f_{crack} is the crack-grade coefficient, f_{length} the rod-length weight and $f_{location}$ the fracture-location weight. The main analysis uses the measured maximum crack width as a continuous variable:

$$HTS = \sum\left(w_{\mathrm{crack}}\, f_{\mathrm{length}}\, f_{\mathrm{location}}\right)$$

The rod-length weights for rods A, B, C and D were 32, 16, 8 and 4, respectively, and the location weights for the column-end (riser-side) junction, the ball end and the rod mid-section were 1, 2 and 3, respectively; this scheme retains the convention that cracking on a short, weakly constrained rod indicates a higher intrinsic susceptibility [18]. The weighting factors and crack positions are illustrated in Figure 2. Because the rod positions represent different constraint and feeding conditions, the analysis was defined a priori at two levels: the all-rod HTS as the primary index, and a short-rod (A + B) score as a pre-specified position-resolved analysis, rather than as a post-hoc exclusion of rods.

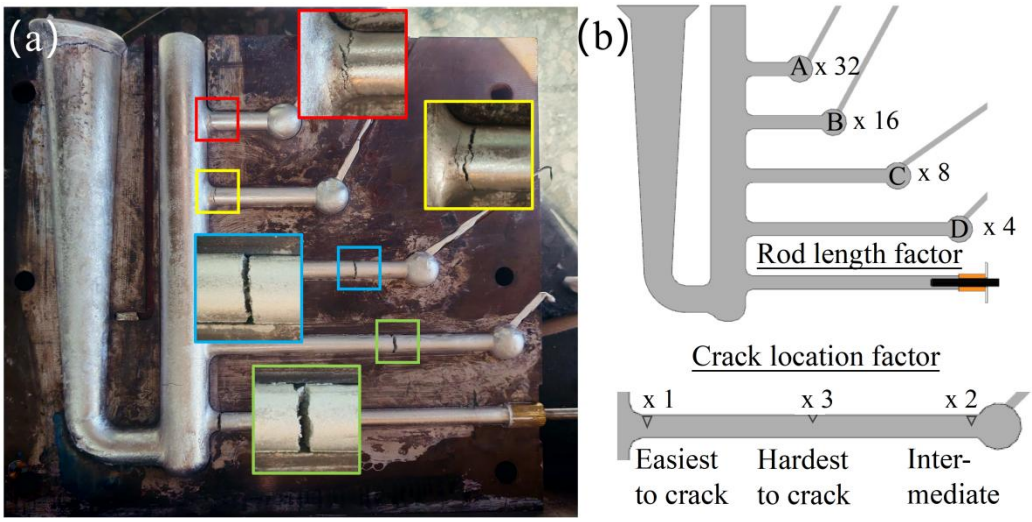


Figure 2. Hot-tearing features and weighting factors used for the ECRC score. (a) Representative casting showing cracks at the different constrained rods with enlarged fracture regions; (b) rod-length factors (A – D: 32, 16, 8, 4) and location factors (column-end junction 1, ball end 2, rod mid-section 3).

2.4 JMatPro calculation and Kou index

JMatPro 13.2 was used to calculate the thermophysical properties, solidification paths and phase fractions of the four measured alloys, providing the temperature-dependent material data for ProCAST. Two composition paths were evaluated to separate the effect of Fe from that of the covarying elements. In the Fe-only scan, Fe was varied from 0.08 to 0.25 wt.% in 0.01 wt.% steps while Zn, Mg, Cu and Zr were fixed at their mean measured contents; this path tests whether Fe variation alone modifies the terminal solidification path. In the second path, the index was calculated directly for the four measured compositions, which retain the actual covariation of Table 1.

Following Kou [10,11], cracking susceptibility was evaluated from the terminal solidification interval $0.90 \leq f_s \leq 0.99$. The temperatures at $f_s = 0.90$ and 0.99 were obtained by linear interpolation of the JMatPro output, and an endpoint secant was calculated as

$$K_{\mathrm{Kou}} = \left|\frac{\Delta T}{\Delta\sqrt{f_s}}\right| = \frac{|T_{0.99} - T_{0.90}|}{\sqrt{0.99} - \sqrt{0.90}}$$

Because f_s is dimensionless, K_{Kou} is reported in °C. A larger K_{Kou} corresponds to a larger temperature drop over the same high-solid-fraction interval and is associated with slower lateral

bridging and longer interdendritic feeding channels [10–13]. The index is used here as a consistent, comparative descriptor of the solidification path; it is not treated as an independent predictor of crack location. Calculated mass-fraction curves of Al_3Fe, Al_2Cu and $MgZn_2$ were examined to interpret the evolution of Fe-rich and late-forming phases.

2.5 ProCAST simulation

The ECRC pouring process was modelled with a three-dimensional thermo-mechanical finite-element model in ProCAST. The geometry reproduces the experimental mold, except that the load-sensor module was removed because it does not participate in solidification heat transfer. Linear tetrahedral elements were used throughout, with a total of 3,999,537 elements and local refinement to 0.5 mm at the rod junctions, 1 mm at the sprue–riser junction, 2 mm in the sprue body and 3 mm in the mold (Figure 3a). The model inputs are listed in Table 2: alloy inlet temperature 710 °C, mold initial temperature 200 °C (the stable pre-pouring temperature, not the earlier 300 °C conditioning step), inlet mass flow 0.275 kg s^{-1}, external convection 10 W m^{-2} K^{-1} at 20 °C, and a termination temperature of 300 °C.

The thermo-mechanical calculation used an elastic–viscoplastic (E-VP) constitutive description, with the Flow, Thermal, Porosity, Stress and hot-tearing modules activated; temperature-dependent properties were computed in JMatPro 13.2 and imported. The casting–mold boundary was represented by a temperature-dependent effective interfacial heat-transfer coefficient (HTC) obtained by inverse calibration: the HTC of successive temperature intervals was adjusted until the simulated T1 history reproduced the mean of the three measured T1 histories for each alloy (Figure 3b and Figure 4). This calibration reproduces the dataset used for the inversion and is therefore not regarded as independent validation. Because previous semi-solid experiments and multi-scale models associate hot tearing with skeleton formation, viscoplastic strain accumulation and bridge fracture [28–30], the response during the late mushy stage ($0.90 \leq f_s < 1$) was evaluated separately from the final simulated state, so that the fully solidified high-stress field was not misinterpreted as the crack-initiation condition.

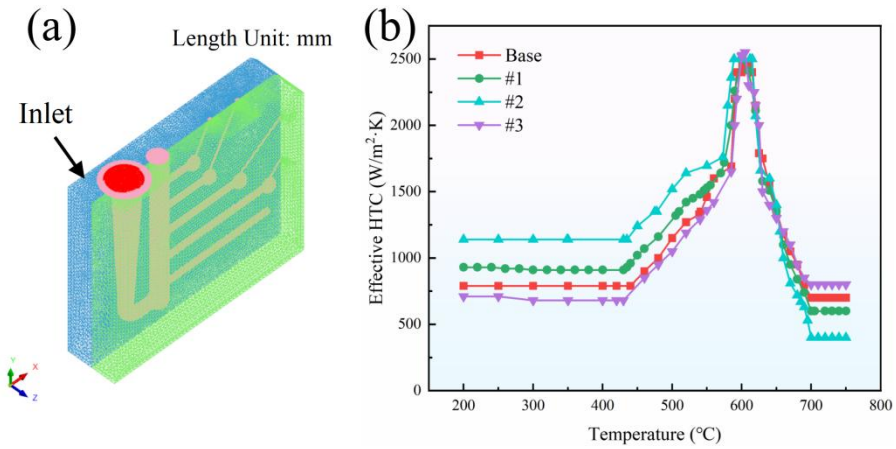


Figure 3. Numerical model and effective heat-transfer boundary for the ProCAST simulation. (a) Finite-element model and mesh of the ECRC mold and casting; (b) temperature-dependent effective interfacial heat-transfer coefficients for the Base, #1, #2 and #3 alloys.

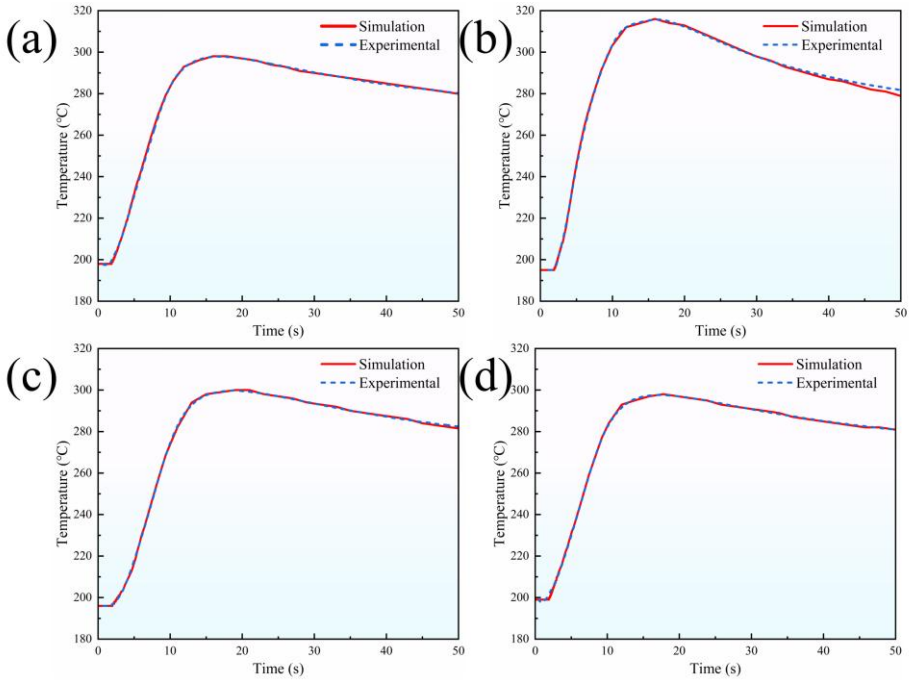


Figure 4. Measured and simulated T1 thermal histories after HTC calibration: (a) Base, (b) #1, (c) #2 and (d) #3 alloy.

Table 2 ProCAST model inputs and numerical settings

Category	Parameter	Value	Unit
Geometry and mesh	Element type	Linear tetrahedral	-
	Total element count	3,999,537	elements
	Local mesh size	0.5 / 1 / 2 / 3	mm
Initial and boundary	Alloy / inlet temperature	710	℃
	Inlet mass flow rate	0.275	kg s-1
	Mold / casting interface HTC	h (T), alloy-specific	W m-2 K-1
Materials and models	Mold material / behavior	H13 steel / rigid	-
	Alloy constitutive behavior	E-VP	-
	Temperature-dependent properties	JMatPro 13.2	-
	Flow model	ON	-
	Thermal / porosity model	ON	-
	Stress / hot-tearing model	ON	-
	Critical solid fraction	0.5	-
Numerical control	Initial time step	0.001	s
	Maximum filling time step	0.1	s
	Maximum time step	1	s
	Termination temperature	300	℃

2.6 Microstructural characterization

Cross-sections adjacent to the fracture of each constrained rod were taken from one ECRC casting per alloy (the third replicate). After sectioning, mounting, grinding and polishing, the crack-adjacent microstructures were examined by backscattered-electron (BSE) imaging, and EDS elemental maps were collected at 500× magnification. EDS mapping was used to confirm Fe enrichment of the bright BSE regions and their spatial relation to interdendritic areas and crack paths; it does not by itself provide crystallographic phase identification.

The area fraction of Fe-enriched regions was quantified with ImageJ. Three representative fields of view were analyzed for each alloy–rod combination and averaged per rod position. These fields are nested observations from one casting per alloy; the measurements therefore describe the trend along the composition series and were not used for alloy-level significance testing.

2.7 Statistical analysis

Casting-level means are reported as mean ± SD over the three independent ECRC trials per alloy. Group differences in the hot-tearing susceptibility were assessed with an exact permutation test, and group differences in peak load with one-way ANOVA, with the rods within a casting treated as nested (non-independent) observations. A value of $p < 0.05$ was considered significant. Because three repetitions provide limited statistical power, non-significant results are interpreted together with the coefficient of variation (CV) and the direction of the effects rather than as evidence of no difference; a sensitivity analysis based on the observed scatter (Section 3.1) indicates the repetition number that would be required to resolve differences of the observed size. All analyses were performed in [software, e.g., R 4.x / Python scipy].

3. Results

3.1 ECRC repeatability and fracture locations

Figure 5a compares the mean crack widths measured on rods A–D across the twelve castings. In rod A, the Base, #1, #2 and #3 alloys exhibited crack widths of 0.587 ± 0.148, 0.722 ± 0.114, 0.482 ± 0.170 and 0.578 ± 0.051 mm, respectively; the corresponding values in rod B were 0.634 ± 0.112, 0.731 ± 0.076, 0.908 ± 0.344 and 0.784 ± 0.072 mm. Cracks opened further on rods C and D, with mean widths of 0.984–1.211 mm on rod C and 1.571–2.221 mm on rod D. For all four alloys the crack width increased from the short rods to the long rods, while the scatter among compositions at a given rod position was substantial.

The spatial distribution reflects the design of the test rather than alloy chemistry. Once solidification shrinkage is arrested by the mold, longer rods accumulate a larger displacement difference and therefore develop wider final openings [14,17]. The crack width measured on a single rod consequently cannot be equated with the intrinsic susceptibility of an alloy; comparisons must be made at identical positions and together with casting-level statistics.

The fracture locations were considerably more repeatable than the crack widths. Across the twelve castings, the column-end junctions of rods A and B fractured in every casting of every alloy (100% fracture frequency), whereas the fracture positions on rods C and D were distributed among the mid-section and the ball-end junction (see the fracture-frequency map in Figure 6d below). This contrast between stable fracture locations and variable crack widths is a characteristic feature of the ECRC test for the present 7xxx alloys and is used below to separate the robust observables from the noisy ones.

Figure 5b presents the casting-level all-rod HTS. The Base, #1, #2 and #3 alloys yielded 67.1 ± 6.7, 74.1 ± 3.8, 68.3 ± 7.9 and 62.7 ± 19.0, respectively. Alloy #1 had the highest mean, whereas alloy #3 had the lowest mean together with by far the largest scatter (CV = 30%, against 5–12% for the other alloys). An exact permutation test detected no significant difference among the four groups ($p = 0.730$). The rod-level decomposition is shown in Figure 6; the mean crack width was 0.698 ± 0.211 mm at the column-end junctions, 1.591 ± 0.575 mm at the rod mid-sections and 1.684 ± 0.462 mm at the ball-end junctions, confirming that the all-rod score is dominated by the long-rod contributions, which are also the least repeatable.

The pre-specified short-rod analysis gave the same qualitative picture. Recalculating the score from rods A and B only yielded 28.9 ± 6.2, 34.8 ± 2.5, 30.0 ± 0.2 and 31.0 ± 0.9 for the Base, #1, #2 and #3 alloys ($p = 0.239$; Figure 7). Both formulations placed alloy #1 in the highest mean range, but neither ranking exceeded the casting-to-casting variability.

To make the resolving power explicit, the largest observed between-alloy difference in the all-rod HTS (#1 versus #3, 11.4 units, Cohen's $d \approx 0.83$) would require approximately twenty repetitions per alloy to reach significance at $\alpha = 0.05$ and 80% power under the observed scatter—far beyond a standard ECRC campaign. The practical implication is that, for this alloy class, the crack-width-based score ranks alloys with limited resolving power at three repetitions, and any interpretation of the composition series must rely on converging evidence from the load signal, the solidification-path calculation and the simulation.

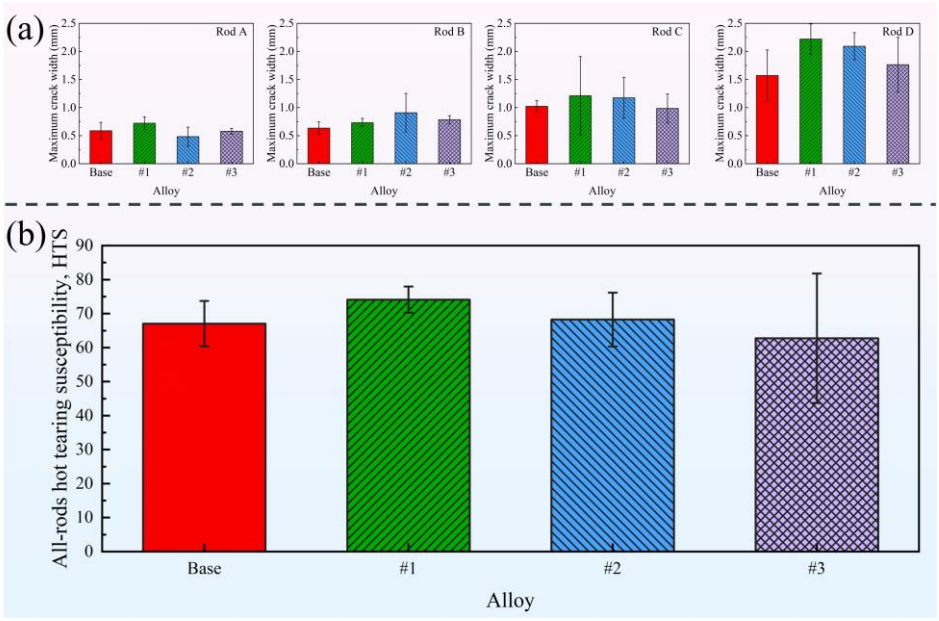


Figure 5. Repeated ECRC results for the four alloys. (a) Maximum crack width of rods A–D; (b) casting-level all-rod hot-tearing susceptibility (HTS).

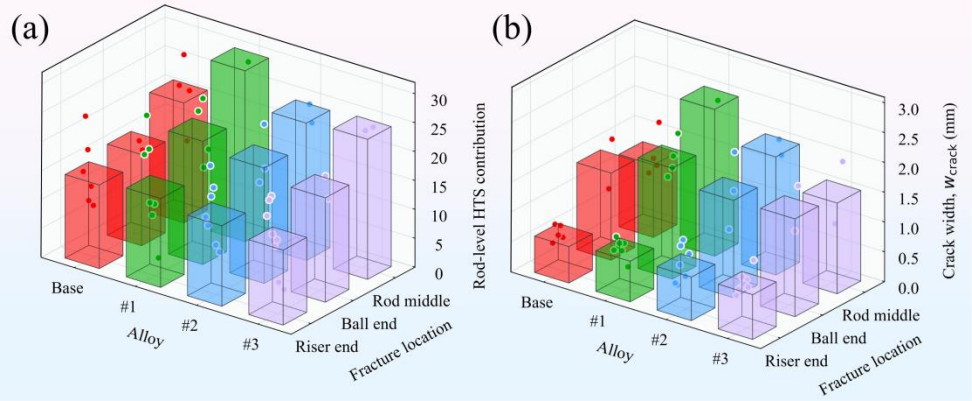


Figure 6. Rod-level decomposition of hot-tearing response from the 12 ECRC tests. (a) Rod-level HTS contribution and (b) crack width as a function of alloy and fracture location.

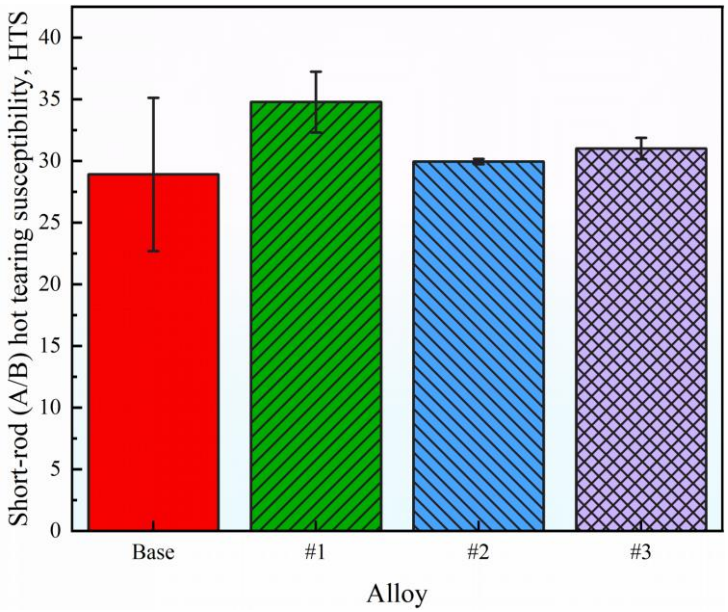


Figure 7. Short-rod hot-tearing susceptibility calculated from rods A and B

3.2 Kou index and the solidification path

Figure 8 compares the Kou index K_{Kou} for the two calculation paths. The Fe-only scan changed only from approximately 1526 to 1532 °C between 0.08 and 0.25 wt.% Fe and was nearly horizontal: with Zn, Mg, Cu and Zr fixed at their mean contents, Fe variation alone did not measurably alter the terminal slope $|\Delta T/\Delta\sqrt{f_s}|$. Direct calculations for the four measured compositions yielded 1775.9, 1846.7, 1683.2 and 1667.3 °C for the Base, #1, #2 and #3 alloys, respectively, ranking alloy #1 highest. The much larger variation along the measured-composition path shows that the co-varying elements dominate the differences in the terminal solidification path.

Figure 9 shows the corresponding $T–\sqrt{f_s}$ curves over the high-solid-fraction interval. The Fe-only curves nearly overlap, whereas the four measured compositions differ in both curvature and temperature drop. The Kou index is therefore used only as a comparative descriptor of the solidification path: the higher value of alloy #1 is directionally consistent with its higher mean HTS and peak load (Sections 3.1 and 3.6), but it reflects the measured multicomponent composition and cannot be ascribed to the Fe content in isolation.

The calculated phase-fraction curves (Figure 10) support this interpretation. Across the four alloys, the calculated maximum Al_3Fe fraction increased monotonically with the Fe content and its formation-onset temperature rose from approximately 590 to 610 °C, while the $MgZn_2$

fraction increased slightly and the Al_2Cu onset temperatures differed by less than about 0.5 °C between alloys. These phase-related differences are modest and gradual; none of them alone reproduces the ranking of the measured hot-tearing response.

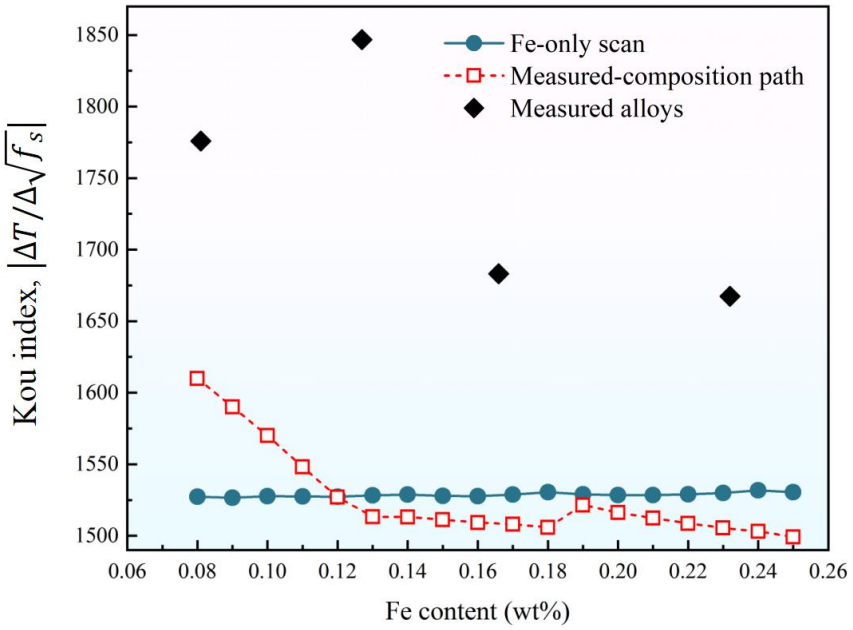


Figure 8. Kou index calculated from the JMatPro solidification data.

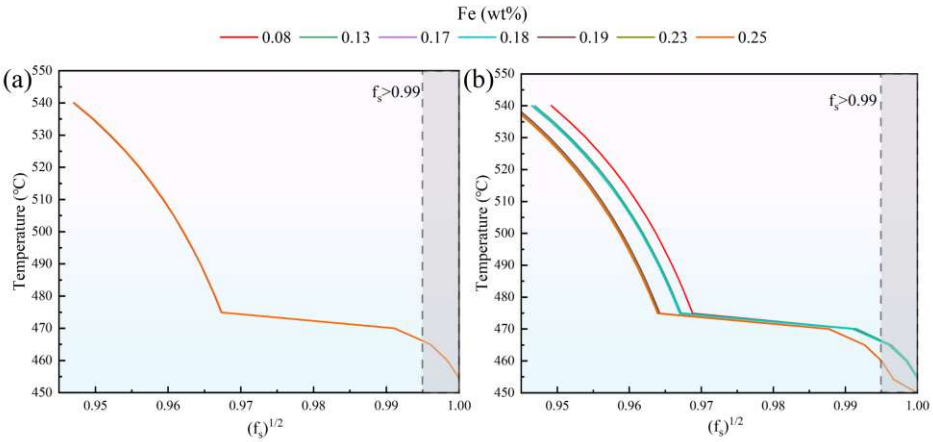


Figure 9. Terminal solidification paths used for the Kou-index calculation. (a) Fe-only scan and (b) measured-series scan plotted as temperature versus solid fraction in the terminal solidification range. The shaded region marks the high-solid-fraction interval used to evaluate the Kou index.

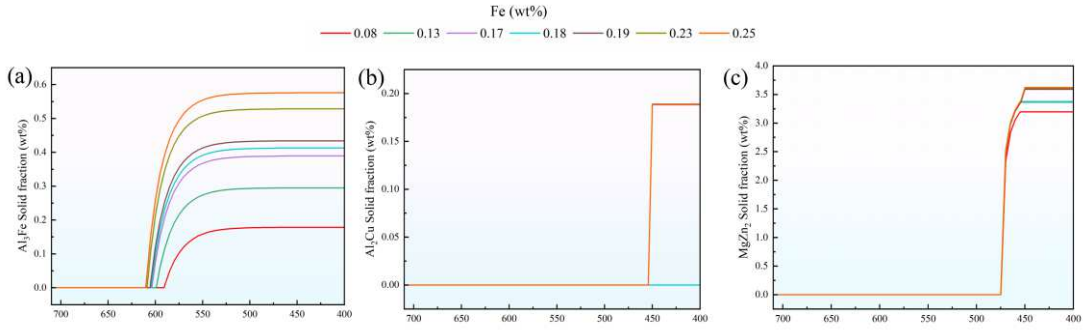


Figure 10. Phase-fraction evolution predicted by JMatPro for the measured-series compositions. (a) Al_3Fe, (b) Al_2Cu, (c) $MgZn_2$.

3.3 Fracture morphology and Fe-rich regions

Figure 11 summarises the SEM fracture morphologies of rods A–D for the four alloys. Cracks propagated predominantly through interdendritic regions. The fracture surfaces contain partially separated solid bridges, torn edges and second-phase particles attached to interdendritic areas; the wider openings on rods C and D agree with the macroscopic measurements in Figure 5a. The BSE images in Figure 12 show bright Fe-enriched regions located mainly along interdendritic zones and adjacent to cracks.

These features are consistent with the accepted picture of hot tearing in the mushy zone: as the dendritic skeleton begins to carry shrinkage strain and the feeding capacity of the residual liquid declines, the interdendritic liquid film is placed under tension, and microvoids coalesce into a macroscopic crack where separation exceeds bridging and feeding [4,5,10,30]. The observed bridges indicate that the solid network had developed partial connectivity before fracture. Static fracture morphology cannot, however, establish the solid fraction at crack initiation, and the number of bridging features in individual fields should not be read as varying monotonically with composition.

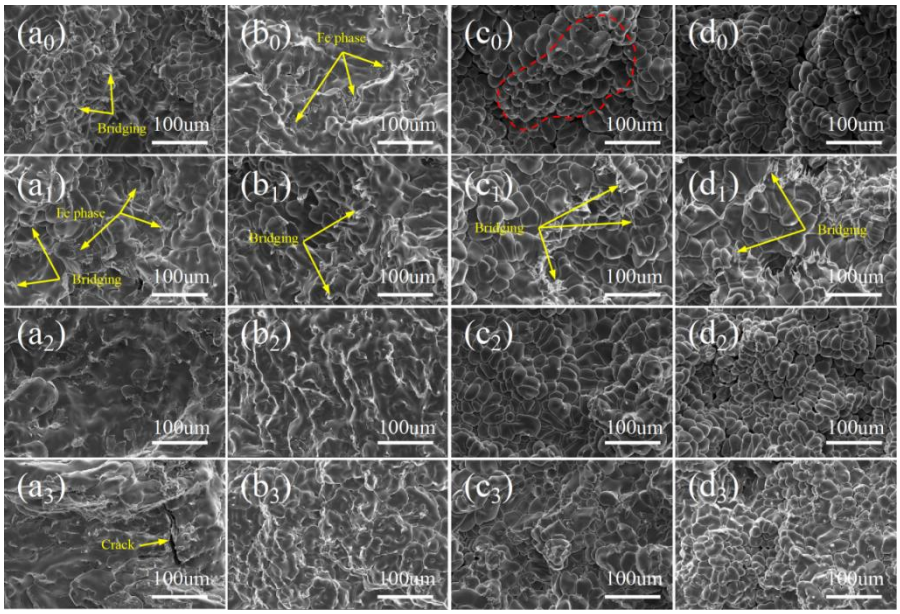


Figure 11. SEM fracture morphologies of the constrained rods in the four measured alloys. Columns correspond to rods A–D and rows correspond to the Base, #1, #2 and #3 alloys. Arrows mark representative cracks, bridging features and Fe-rich particles near the hot-tearing fracture surfaces.

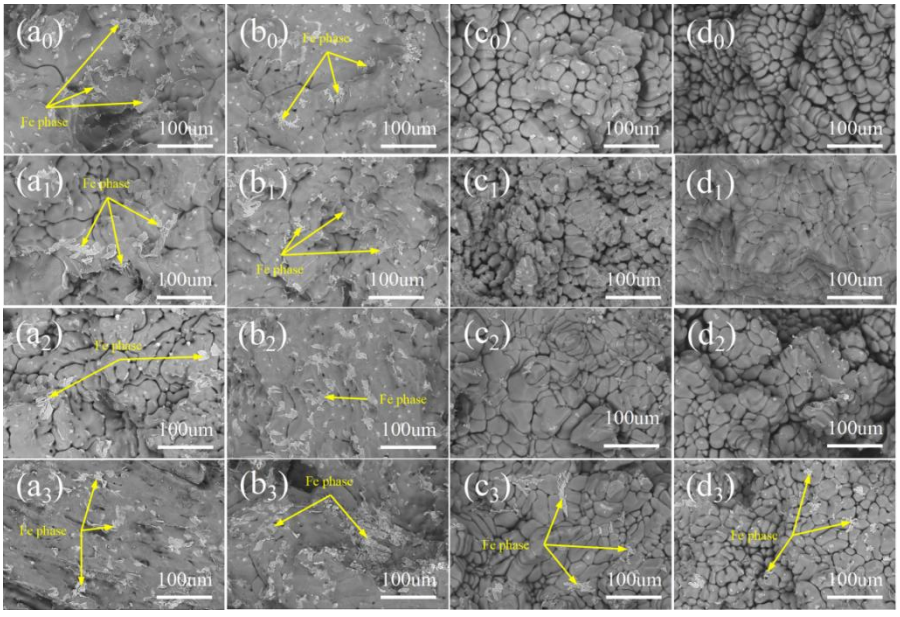


Figure 12. BSE images of cross-sections adjacent to fractures in rods A–D of the Base, #1, #2 and #3 alloys. Bright BSE regions enriched in Fe are located near interdendritic cracks and fracture-related features.

Figure 13 quantifies the Fe-enriched area fraction in crack-adjacent sections of one casting per alloy. The alloy-level means were 0.491%, 0.546%, 0.779% and 0.846% for the Base, #1, #2 and #3 alloys, increasing overall with the measured Fe content; differences among rod positions remained within the same casting (for example, 0.331–0.600% across the rods of the Base alloy). The BSE images and EDS maps in Figure 14 confirm the Fe enrichment of the bright regions, with varying degrees of Cu partitioning. Notably, the monotonic increase of the Fe-enriched area fraction does not follow the non-monotonic HTS ranking: alloy #3 had the largest Fe-enriched area fraction but the lowest mean HTS, whereas alloy #1 combined an area fraction only slightly above that of the Base alloy with the highest mean HTS, Kou index and peak load. The amount of Fe-enriched material is therefore not, by itself, the controlling variable; its influence must depend on morphology, continuity and the spatial relation to the late-stage liquid, as reported for other alloy systems [21–24].

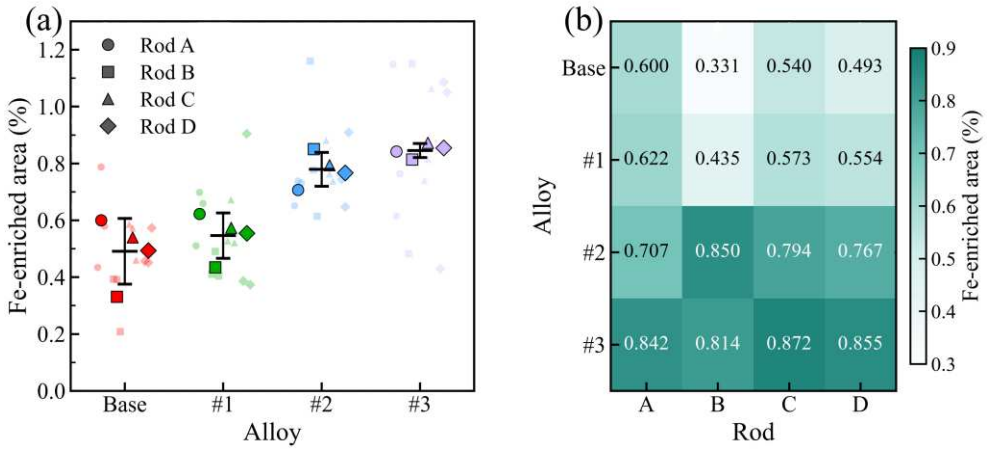


Figure 13. Quantification of Fe-enriched area fraction near the crack regions. (a) Fe-enriched area fraction measured from SEM/EDS elemental maps at 500× magnification for rods A–D in each alloy. (b) Heat map of the rod-averaged Fe-enriched area fraction.

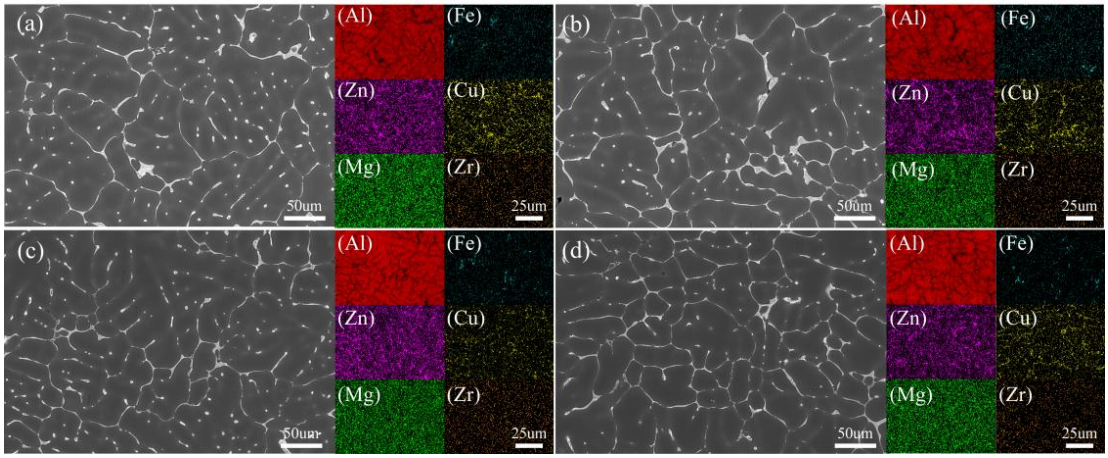


Figure 14. Representative BSE images and EDS elemental maps near the crack regions. (a) Base alloy, (b) #1 alloy, (c) #2 alloy, (d) #3 alloy.

3.4 Solidification sequence and mushy-stage response

Figure 15 presents the simulated temperature and solid-fraction fields of the Base alloy at 6.10, 14.20, 19.95, 37.95 and 63.95 s after pouring, corresponding to overall solid fractions of approximately 21.5%, 67.6%, 80.5%, 92.6% and 98.2%. Solidification began at the outer surfaces and in the thin rod sections in contact with the mold and then advanced towards the casting interior and the local hot spots. The thin rods developed a continuous solid skeleton early, while the junctions and thicker sections retained liquid; the subsequent shrinkage could not be accommodated freely because both rod ends were constrained. Mechanical constraint was therefore established before the residual liquid was consumed, providing the thermal basis for the strain concentration near the column-end junctions and for the larger final openings on rods C and D. This staged response—skeleton formation first, deformation accumulation later—is consistent with semi-solid experiments and multi-scale models of AA7050-type alloys [28–30].

Figure 16 compares the duration of the late mushy stage ($0.90 \leq f_s < 1$), the peak effective stress, the peak effective plastic strain and the hot-tearing indicator (HTI) extracted at identical locations for the four alloys. The column-end junctions remained in this interval for approximately 12–20 s, whereas the mid-sections and ball-end junctions of rods C and D remained for only 2.5–6.6 s. The peak effective stress within the window ranged from 13.7 to 23.8 MPa, and the peak effective plastic strain at the column-end junction of rod A ranged from 0.044 to 0.063. Residence time, stress and plastic strain did not peak simultaneously at every position, indicating that the late-stage risk is set jointly by the local thermal history and the

mechanical constraint. The software-defined HTI was zero at several positions within the interrogated window; this only means that the indicator was not activated there and does not demonstrate the absence of risk, so the residence time and accumulated plastic strain are used as the more direct descriptors.

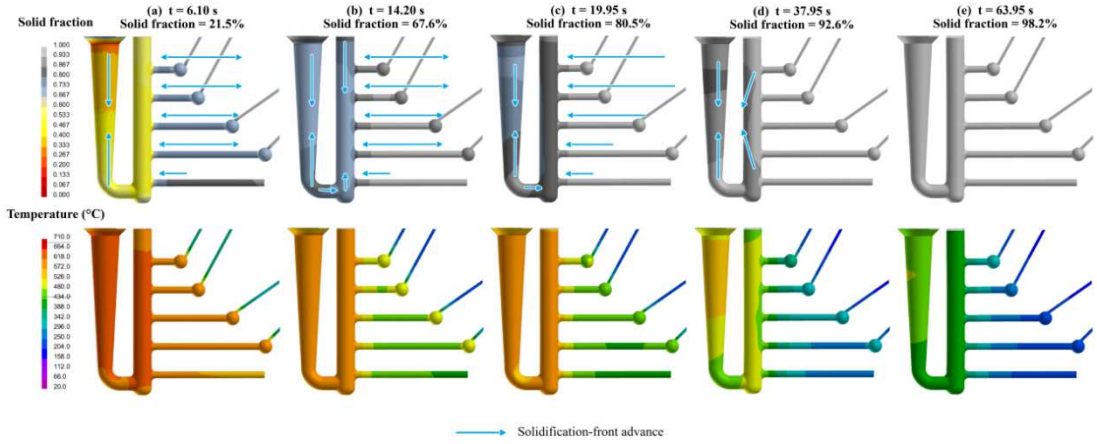


Figure 15. ProCAST-predicted solidification trend of the Base alloy in the ECRC geometry. Solid fraction and temperature fields are shown at representative times from early filling/solidification to the final high-solid-fraction stage.

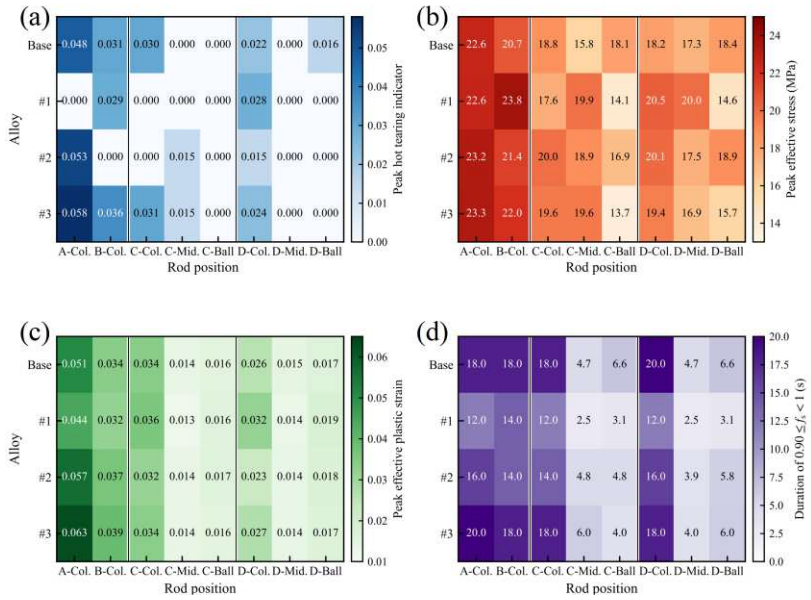


Figure 16. ProCAST metrics extracted during the late mushy stage. (a) Peak hot-tearing indicator, (b) peak effective stress, (c) peak effective plastic strain and (d) duration of the interval at the selected rod locations.

3.5 Simulated state versus fracture frequency

Figure 17a–c presents the final HTI, effective stress and effective plastic strain at the characteristic locations, and Figure 17d the fracture frequencies from the twelve ECRC trials. The final effective stress reached 565–658 MPa at the column-end junction of rod A, 471–501 MPa at that of rod B and 333–363 MPa at that of rod C, with 159–214 MPa at most remaining locations. Experimentally, the column-end junctions of rods A and B fractured in all twelve castings (100%), coinciding with the strongest simulated stress and strain concentrations; the fracture frequencies on rods C and D were dispersed and corresponded only partly to the simulated high-value regions.

The agreement at the A/B junctions shows that the E-VP model identifies the regions of dominant geometric constraint. The discrepancies at rods C and D indicate that the final field is not a snapshot of crack initiation: once a crack forms, the local stiffness, contact and load-transfer paths change, and the present model does not describe crack propagation or its feedback. The final fields therefore quantify the accumulated constraint at the end of the calculation, while crack initiation is interpreted through the late-mushy-stage response of Section 3.4 together with the measured fracture locations [29,30].

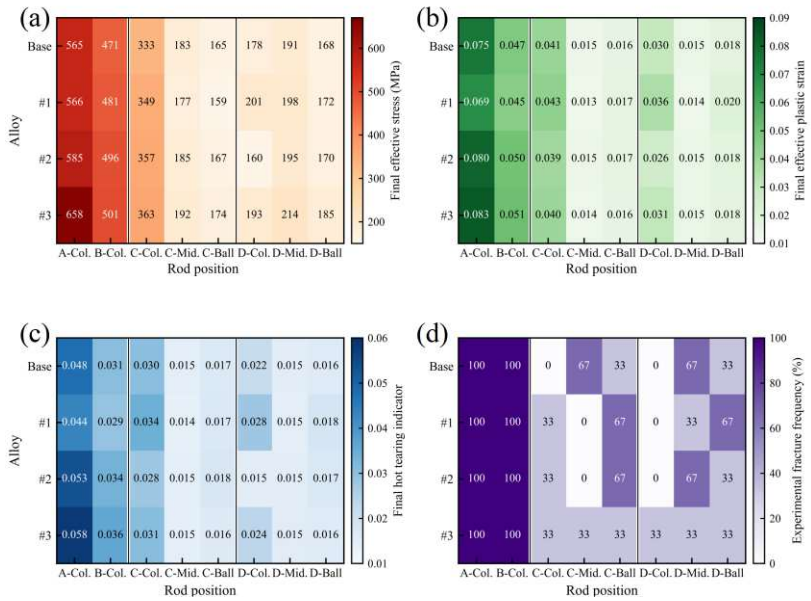


Figure 17. Final simulated thermo-mechanical state and experimental fracture frequency. (a) Final effective stress, (b) final effective plastic strain, (c) final hot-tearing indicator and (d) experimental fracture frequency from three ECRC repetitions at the selected rod locations.

3.6 Contraction-load response

Figure 18 shows the load–time and temperature–time histories. Each alloy exhibited a major load peak approximately 5–9 s after pouring, followed by a gradual decrease. The dendrite coherency point (DCP) temperatures determined from the temperature curves were approximately 636, 634, 635 and 635 °C, and the crack-related characteristic temperatures were approximately 471, 472, 472 and 477 °C for the Base, #1, #2 and #3 alloys, respectively. The mean peak loads were 70.2 ± 13.2, 87.2 ± 3.2, 65.5 ± 8.5 and 68.9 ± 9.0 N (Table 3); one-way ANOVA on the casting-level means gave $p = 0.077$.

Two features make the load signal practically valuable for this alloy class. First, it was more repeatable than the crack-width-based score: the CV of the peak load was 3.7–19% against up to 30% for the all-rod HTS, and alloy #1 combined the highest mean peak load (24% above the Base alloy) with the smallest scatter. Second, the direction of the load ranking agrees with the Kou index of Section 3.2 and with the HTS means of Section 3.1, so three independent observables converge in placing alloy #1 at the top of the measured series. The rapid load increase reflects the onset of force transmission once the dendritic network becomes coherent, and the post-peak decrease combines thermal-contraction changes, local plastic relaxation and the loss of load-bearing capacity after cracking [4,31]. The peak load nevertheless also depends on the force-rod geometry and the thermal history, and at $p = 0.077$ it should be read as a strong but not fully conclusive discriminator at three repetitions.

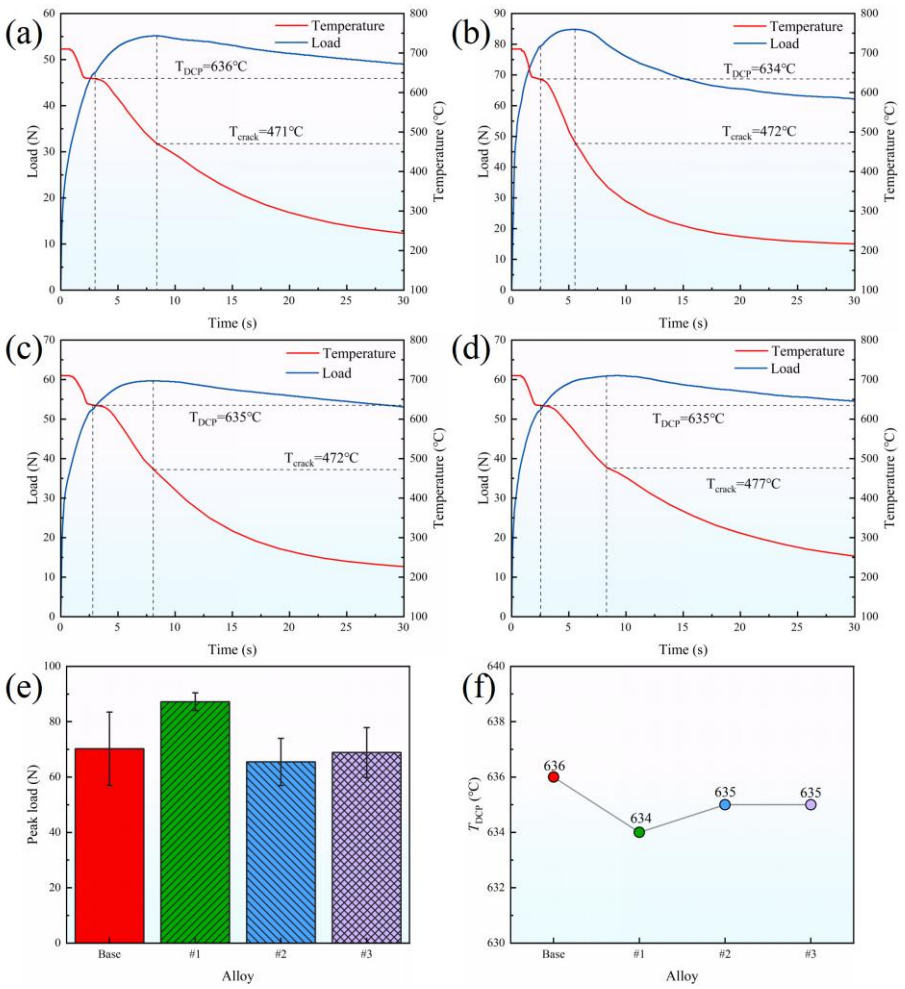


Figure 18 Load and temperature responses during ECRC solidification. (a-d) Representative load and temperature histories for the Base, #1, #2 and #3 alloys, with the dendrite coherency point temperature T_{DCP} and crack-related temperature T_{crack} marked. (e) Peak load statistics from repeated experiments. (f) T_{DCP} values of the four alloys.

4. Discussion

4.1 Resolving power of the ECRC test

The twelve instrumented castings separate the ECRC observables into two groups with different information content. The fracture locations and the load response were highly repeatable: the A/B column-end junctions fractured in 100% of the castings, the DCP temperatures were confined to 634–636 °C, and the peak load ranked the alloys consistently. The crack widths and the derived HTS, by contrast, carried large casting-to-casting variability (CV up to 30%), and the between-alloy differences did not reach significance ($p = 0.730$). For wide-

freezing-range 7xxx alloys—whose long vulnerable interval amplifies small differences in filling and thermal history—the ECRC test therefore remains applicable, but its resolving power at three repetitions lies in the fracture-location statistics and the load signal rather than in the crack-width score. Users of the method for this alloy class should report position-resolved fracture frequencies and load statistics alongside, or instead of, a single HTS number, and should state the casting-level scatter explicitly.

This reading also clarifies the relation to earlier ECRC/CRC studies on A206, A380 and Al–Cu alloys [14–17]. In those narrower-range systems the crack-grade score discriminated alloys at comparable repetition numbers; the present data suggest that the wider freezing range of 7xxx alloys shifts more of the response into the variability of the long rods, so the scoring scheme transfers but the experimental effort required for a given resolution increases.

4.2 Short-rod versus long-rod response

The simulation explains why the A/B and C/D responses must be interpreted separately, and this separation follows from the mold geometry rather than from any data selection. The thin rods solidify early and develop a continuous skeleton, while the column-end junctions remain in the late mushy stage for 12–20 s under restraint, accumulating the highest plastic strain; these junctions fractured in every casting, and their response therefore reflects the alloy behavior under the most severe but well-fed constraint. The long rods C and D solidify first at mid-length (Figure 15), which interrupts the feeding path from the riser side; their dispersed fracture positions and large openings are dominated by this feeding cut-off and by the accumulated displacement of the long lever arm, i.e. by geometry rather than by alloy chemistry [17]. This is consistent with the stress fields of Section 3.5, where the simulated concentrations matched the experiments at A/B but only partly at C/D.

The pre-specified short-rod score (Section 3.1) is thus not a correction of the all-rod score but a position-resolved complement: the all-rod HTS describes the total severity of cracking in the casting, while the A/B response, the fracture frequencies and the load signal describe the alloy-dependent part most reproducibly. Reporting both levels, with their scatter, avoids two opposite misreadings of ECRC data—over-interpreting the noisy long-rod contributions and discarding information by excluding rods after the fact.

4.3 Converging evidence along the composition path

Although no single observable reached statistical significance at three repetitions, three independent measurements point in the same direction for the present series: alloy #1 (0.127 wt.% Fe) gave the highest mean all-rod HTS, the highest and most repeatable peak load, and the highest Kou index. The Kou analysis further shows that this ranking cannot be produced by Fe variation alone—the Fe-only scan was essentially flat—and must therefore be attributed to the measured multicomponent path, in which Zn, Mg and Cu co-vary with Fe. The BSE/EDS quantification adds a second decoupling: the Fe-enriched area fraction increased monotonically (0.491 → 0.846%) without following the HTS ranking, so the amount of Fe-rich phase is not the controlling factor within this window. The picture that emerges is consistent with the mechanism reported for Al–Cu and Al–Mg–Si systems [21–24]: the hot-tearing response is governed by how the whole solidification path—terminal liquid films, Fe-rich phase morphology and continuity, bridging and feeding—interacts with the constraint, rather than by any single element or phase fraction. Practically, the present data support treating the 0.081–0.232 wt.% Fe window as a region in which process variability and the accompanying major-element variations matter at least as much as Fe itself; they do not support a composition threshold.

4.4 Limitations

Several limitations bound the interpretation. Only three ECRC trials per alloy were performed; a power estimate based on the observed scatter indicates that substantially more repetitions would be required to resolve differences of the observed size, so the non-significant group tests should be read as “not resolved at this repetition number” rather than as evidence of identical behavior. The four alloys follow a measured composition path in which Zn, Mg and Cu co-vary with Fe, and the design cannot isolate a pure Fe effect experimentally; the Fe-only calculation addresses this analytically but not metallurgically. Grain size, a strong lever on hot tearing [31,32], was not measured and is a potential confounder despite the identical refiner practice. The HTC is an effective inverse-calibrated boundary and its alloy-to-alloy differences partly absorb fitting freedom. The microstructural quantification used nested fields from one casting per alloy. Finally, the E-VP properties were taken from the JMatPro database without alloy-specific semi-solid mechanical calibration [28], so absolute simulated stresses are comparative rather than predictive values.

5. Conclusions

(1) Twelve replicated ECRC castings of four 7xxx Al–Zn–Mg–Cu alloys show that the test is applicable to this wide-freezing-range alloy class, but its robust observables are the fracture-location statistics (A/B column-end junctions fractured in 100% of castings) and the contraction-load signal, whereas the crack-width-based HTS carried up to 30% casting-to-casting variability.

(2) The short rods (A, B) and long rods (C, D) measure different things: the A/B junctions combine long late-mushy residence (12–20 s) with high accumulated plastic strain and reflect the alloy response under severe, well-fed constraint, whereas rods C and D solidify first at mid-length, suffer feeding cut-off and give geometry-dominated, dispersed fractures. Position-resolved reporting of both levels is recommended when applying ECRC to 7xxx alloys.

(3) Along the measured composition path (0.081–0.232 wt.% Fe with co-varying Zn, Mg and Cu), alloy #1 ranked highest in all-rod HTS (74.1 ± 3.8), peak load (87.2 ± 3.2 N) and Kou index (1846.7 °C), but the group differences did not exceed the experimental variability ($p = 0.730$ for HTS; $p = 0.077$ for peak load). The Fe-only solidification scan was nearly invariant (1526–1532 °C) and the Fe-enriched area fraction increased monotonically (0.491 → 0.846%) without following the HTS ranking, showing that the response is governed by the multicomponent solidification path rather than by Fe content or Fe-rich phase amount alone.

(4) The E-VP ProCAST model reproduced the experimentally observed high-risk locations at the A/B column-end junctions and explained the long-rod behavior through the solidification sequence; agreement at rods C and D was only partial because the model does not describe crack propagation and its feedback.

(5) For industrial alloy series of this type, the results indicate that within 0.081–0.232 wt.% Fe the differences in hot tearing are smaller than the variability of a standard three-repetition ECRC test; conclusions about composition effects at this level require more repetitions and complementary load-based evaluation, and no Fe control threshold can be derived from the present data.

Acknowledgments

This research was supported by Southwest United Graduate School (Grant no. 202502AO070008), the Key Research & Development Program of Yunnan Province (Grant no. 202503AA080029) and the Key Science and Technology Project of Yunnan Province (Grant no. 202402AB080012).

References

[1] Li P, Sui Y, Jiang Y, et al. Optimizing hot tearing susceptibility of Al-5.5Zn-2.4Mg-1.3Cu alloys by grain refinement, increasing mold and casting temperature. Materials & Design, 2024, 246: 113325.

[2] Zhou B, Liu B, Zhang S. The advancement of 7xxx series aluminum alloys for aircraft structures: A review. Metals, 2021, 11(5): 718.

[3] Park S, Lee J, Jeon J, et al. Microstructural evolution during homogenization of direct-chill-cast Al-Zn-Mg-Cu alloy. Metals and Materials International, 2025, 31(5): 1323-1333.

[4] Li Y, Li H, Katgerman L, et al. Recent advances in hot tearing during casting of aluminium alloys. Progress in Materials Science, 2021, 117: 100741.

[5] Eskin D G, Katgerman L. Mechanical properties in the semi-solid state and hot tearing of aluminium alloys. Progress in Materials Science, 2004, 49(5): 629-711.

[6] Bing Z, Shuai L, Kai-Le X, et al. Hot cracking tendency test and simulation of 7075 semi-solid aluminium alloy. Transactions of Nonferrous Metals Society of China, 2020, 30(2): 318-332.

[7] Clyne T W, Davies G J. The influence of composition on solidification cracking susceptibility in binary alloy systems. British Foundryman, 1981, 74(4): 65-73.

[8] Katgerman L. A mathematical model for hot cracking of aluminum alloys during DC casting. JOM, 1982, 34(2): 46-49.

[9] Rappaz M, Drezet J M, Gremaud M. A new hot-tearing criterion. Metallurgical and Materials Transactions A, 1999, 30(2): 449-455.

[10] Kou S. A criterion for cracking during solidification. Acta Materialia, 2015, 88: 366-374.

[11] Kou S. A simple index for predicting the susceptibility to solidification cracking. Welding Journal, 2015, 94(12): 374s-388s.

[12] Liu J, Kou S. Effect of diffusion on susceptibility to cracking during solidification. Acta Materialia, 2015, 100: 359-368.

[13] Liu J, Kou S. Susceptibility of ternary aluminum alloys to cracking during solidification. Acta Materialia, 2017, 125: 513-523.

[14] Hamadellah A, Bouayad A, Gerometta C. Hot tear characterization of AlCu5MgTi and AlSi9 casting alloys using an instrumented constrained six rods casting method. Journal of Materials Processing Technology, 2017, 244: 282-288.

[15] Dubey S N. Design and evaluation of an enhanced constrained rod casting mold for experimental characterization of hot tearing in aluminium casting alloys. International Journal of Cast Metals Research, 2017, 30(4): 201-216.

[16] Dubey S N. Study of hot tearing evaluation methods and quantification of contraction forces in die casting alloys. PhD thesis, The Ohio State University, Columbus, 2015.

[17] Rajagukguk K, Suyitno S, Saptoadi H, et al. Evaluation of horizontal and vertical constrained rod casting mold on hot tearing susceptibility of Al-Cu alloys. International Journal of Metalcasting, 2024, 18(4): 3329-3341.

[18] Argo D, Pekguleryuz M, Vermette P, et al. Hot-tearing assessment using constrained casting. In: Die Casting 2001. North American Die Casting Association, Chicago, 2001: 181-186.

[19] Wu G, Zhao J, Peng Y, et al. Effect of pouring temperature on microstructure, tensile properties and hot-tearing susceptibility of a die-cast Al-Zn-Mg-Cu alloy. International Journal of Metalcasting, 2023, 17(1): 455-465.

[20] Shi H, Bai L, Zhang X, et al. Research on the influence of casting process on hot tearing tendency of 7050 aluminum alloy. International Journal of Metalcasting, 2025, 19(5): 2774-2787.

[21] Kamga H K, Larouche D, Bournane M, et al. Hot tearing of aluminum-copper B206 alloys with iron and silicon additions. Materials Science and Engineering: A, 2010, 527(27-28): 7413-7423.

[22] Sweet L, Easton M A, Taylor J A, et al. Hot tear susceptibility of Al-Mg-Si-Fe alloys with varying iron contents. Metallurgical and Materials Transactions A, 2013, 44(12): 5396-5407.

[23] Ganjehfard K, Taghiabadi R, Noghani M T, et al. Tensile properties and hot tearing susceptibility of cast Al-Cu alloys containing excess Fe and Si. International Journal of Minerals, Metallurgy and Materials, 2021, 28(4): 718-728.

[24] Liang K Y, Huang H C, Tseng C Y, et al. Effects of Fe, Si, Cu, and TiB2 grain refiner amounts on the hot tearing susceptibility of 5083, 6061, and 7075 aluminum ingots. Metals, 2024, 14(1): 15.

[25] Yan Y J, Wu M D, Xiao D H, et al. Effect of Fe content on microstructure and properties of 7075 aluminum alloy. Special Casting & Nonferrous Alloys, 2024, 44(4): 551-558. (in Chinese)

[26] She H, Shu D, Chu W, et al. Effects of Fe and Si impurity elements on microstructure and properties of 7xxx high-strength aerospace aluminum alloys. Journal of Materials Engineering, 2013(6): 92-98. (in Chinese)

[27] She H. Effects of Fe and Si impurities on microstructure and mechanical properties of 7055 aluminum alloy. PhD thesis, Shanghai Jiao Tong University, Shanghai, 2017. (in Chinese)

[28] Subroto T, Eskin D G, Miroux A, et al. Semi-solid constitutive parameters and failure behavior of a cast AA7050 alloy. Metallurgical and Materials Transactions A, 2021, 52(2): 871-888.

[29] Li L, Zhang R, Yuan Q, et al. An integrated approach to study the hot tearing behavior by coupling the microscale phase field model and macroscale casting simulations. Journal of Materials Processing Technology, 2022, 310: 117782.

[30] Liu W, Li G, Lu J. Modeling solidification cracking: A new perspective on solid bridge fracture. Journal of the Mechanics and Physics of Solids, 2024, 188: 105651.

[31] Li Y, Bai Q L, Liu J C, et al. The influences of grain size and morphology on the hot tearing susceptibility, contraction, and load behaviors of AA7050 alloy inoculated with Al-5Ti-1B master alloy. Metallurgical and Materials Transactions A, 2016, 47(8): 4024-4037.

[32] Bai Q L, Liu J C, Li H X, et al. A modified hot tearing criterion for direct chill casting of aluminium alloys. Materials Science and Technology, 2016, 32(8): 846-854.

[33] Guo Y, Qi F, Zhang L, et al. Achieving low hot tearing susceptibility in high-strength cast Al-Li alloys: Experimental investigation and simulation assessment. Materials Science and Engineering: A, 2024, 910: 146901.

[34] Lalpoor M, Eskin D G, Katgerman L. Fracture behavior and mechanical properties of high strength aluminum alloys in the as-cast condition. Materials Science and Engineering: A, 2008, 497(1-2): 186-194.